JOURNAL OF SPACECRAFT AND ROCKETS
Vol. 32, No. 4, July–August 1995

Flow Quality of Hypersonic Wind-Tunnel Nozzles Designed Using Computational Fluid Dynamics

John J. Korte* and Jeffrey S. Hodge†
NASA Langley Research Center, Hampton, Virginia 23681

A new methodology has been demonstrated for designing the aerodynamic contour of hypersonic wind-tunnel nozzles using a computational fluid-dynamics-based design and optimization procedure. The new design method was based on a least-squares parabolized Navier–Stokes design and optimization procedure developed by the first author. An optimization problem was solved using the new design method to determine the aerodynamic contour that minimized the flowfield Mach-number variation. Two existing wind-tunnel nozzles were remachined with the new aerodynamic contours designed with this procedure. The flow quality of the nozzles was examined using detailed pitot-pressure profiles measured in the test section. The flow quality of the remachined nozzles showed an improvement over a recently designed and constructed wind-tunnel nozzle based on the classical method-of-characteristics boundary-layer correction technique. However, the flow quality was not as uniform as predicted, because of disturbances emanating from mechanical joints. The pitot-pressure profile away from the disturbance was extremely uniform, significantly better than for previous wind-tunnel nozzles at similar Mach numbers, demonstrating the importance of using a computational-based design procedure for wind-tunnel nozzles that have to operate with thick boundary layers.

Nomenclature

a_i	= coefficients of cubic spline
b	= volumetric gas constant
c_p	= specific heat at constant pressure
f	= least-squares error vector
f_I	= component of f
I	= index of f
i	= grid index, axial direction
$i_{\max}$	= total number of grid points, axial direction
j	= grid index, y direction
$j_{\max}$	= total number of grid points, y direction
M	= Mach number
M_{axis}	= design centerline Mach number
M_c, M_{design}	= test-section design Mach number
M_x	= computed axial Mach number
m	= total number of components in f
n	= total number of components in X
N	= total number of knots on the cubic spline
Obj	= design objective function
p	= pressure
Pr_t	= turbulent Prandtl number
r^*	= nozzle throat radius, in.
R	= gas constant for helium
R_c	= (throat radius of curvature)/r^*
T	= temperature
W_M, W_{MA}, W_ϕ	= weighting factors
X	= design parameter vector
X_I	= component of X
x	= axial coordinate, in.
x_{0-N}	= axial coordinate of spline knots, in.
y	= Cartesian or radial coordinate, in.
y_w	= nozzle wall coordinate, in.
y^+	= turbulence Reynolds number
β	= grid stretching parameter
η	= crossflow transformation coordinate
θ_a	= subsonic approach angle, deg
θ_{super}	= nozzle inflection angle, deg
μ	= laminar viscosity
ξ	= streamwise transformation coordinate
ρ	= density
ϕ	= flow angle

Subscripts

t	= total conditions for p and T
E	= beginning of source flow region
B	= end of source flow region

Presented as Paper 94-2544 at the AIAA 18th Aerospace Ground Testing Conference; received July 8, 1994; revision received Jan. 31, 1995; accepted for publication March 7, 1995.

*Senior Research Scientist, Mail Stop 159, Multidisciplinary Design Optimization Branch, Fluid Mechanics and Acoustics Division. E-mail: j.j.korte@larc.nasa.gov. Senior Member AIAA.

†Aerospace Engineer, Mail Stop 395, Aerothermodynamics Branch, Gas Dynamics Division.

Introduction

THE aerodynamic lines of two hypersonic wind-tunnel nozzles were designed and tested to demonstrate a new design methodology based on computational fluid dynamics (CFD). The new nozzle coordinates were machined into surplus nozzle assemblies and then tested in NASA Langley's 22-in. helium tunnel. The flow quality of the nozzles was determined by assessing the measured test section pitot pressure profile uniformity. The pitot pressure measurements of the new nozzles were compared with the computed predictions and with pitot pressure measurements produced from a nozzle designed using classical methods. The purpose of the CFD-based design procedure was to improve the flow quality for hypersonic nozzles that operate with large boundary layers. This paper presents the first measurements made of the flow quality obtained with a hypersonic wind-tunnel nozzle designed using a CFD-based optimization procedure.

The paper will present 1) the comparison of the CFD prediction codes against existing data for a Mach 20 helium nozzle, 2) CFD-based design of Mach 14.6 and Mach 20 helium nozzles, 3) experimental calibration data for the new nozzles, and 4) comparison of the CFD predictions with the experimental calibration data.

Hypersonic Wind-Tunnel Nozzle Design

Regardless of the computational advances in fluid mechanics made in the last 60 years, the state of the art in aerodynamic design of supersonic–hypersonic wind-tunnel nozzles has, until recently, been

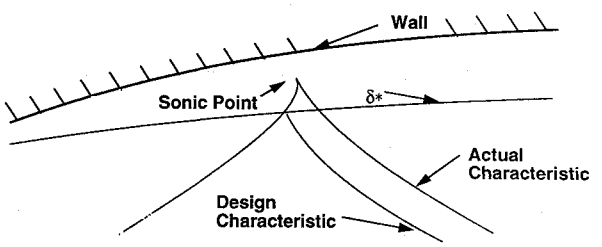

Fig. 1 Path of actual characteristics in a nozzle with a thick boundary layer.

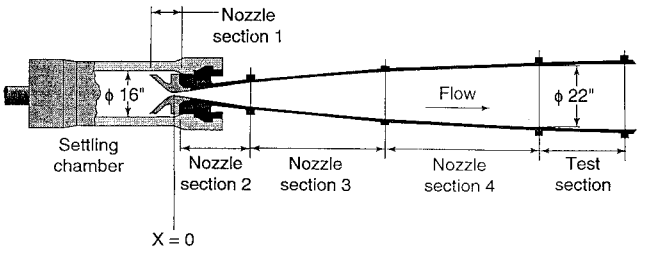

Fig. 2 Nozzle layout for the 22-in. helium tunnel.

based on the method originally proposed by Prandtl and Buseman[1] in 1929. This classical procedure requires that the inviscid contour be designed using the method of characteristics (MOC) and corrected with a displacement thickness obtained from a boundary-layer (BL) solution. Typical improvements in wind-tunnel nozzle design were only refinements or improvements of the MOC–BL procedure. In recent years, new nozzles have been designed using this classical method and evaluated using Navier–Stokes flow solutions.[2] CFD solutions have shown good agreement with the design for Mach numbers up to 8.[3] Unfortunately, the flow quality of the MOC–BL wind-tunnel nozzle is poor when the BL becomes large compared to the inviscid core.[4] For large BLs, typical of hypersonic wind-tunnel nozzles, Candler and Perkins[5] showed that the characteristics reflect between the wall and the location of the inviscid contour (Fig. 1). Therefore, the actual characteristics of the nozzle lagged the characteristics used in the design procedure. In thick boundary layers, the actual characteristics are no longer properly canceled, and the flow quality of the nozzle deteriorates. To improve the flow quality for wind-tunnel nozzles with thick BLs, the development of a new design strategy was required.

Fortunately, the speed and accuracy of CFD flow solvers and the speed of computers have improved significantly in the last decade. Traditionally, CFD codes have been used to investigate new designs or particular flow phenomena. The increase in speed and accuracy has enabled researchers to develop CFD-based design methods that can be used to directly develop the aerodynamic designs. This is a significant improvement, since the design can be based on a CFD computer program that includes complex physical modeling, which is difficult to incorporate into classical design methods. The most powerful and general of the CFD design procedures are based on a solution to an optimization problem.

Recently, Korte et al.[6] coupled a nonlinear least-squares (LS) optimization procedure[7] with an efficient CFD flow solver[8] for the parabolized Navier–Stokes (PNS) equations, which allowed the optimization of the exit flow profile of a MOC–BL-designed nozzle. More recently, Korte[9,10] improved the procedure so that it could be used for the optimum design of a complete nozzle flowfield, without starting from a MOC–BL-designed nozzle. The centerline Mach-number distribution was optimized along with the exit Mach number and flow angle. The equations for defining the centerline Mach number distribution used in the objective function were based on the derivations given by Sivells.[11] The wall is defined using cubic splines whose nodal slopes are obtained from the solution of the optimization problem. This new method can be used to design hypersonic wind-tunnel nozzles with thick BLs, which have excellent flow quality according to numerical flow predictions. In addition, this method is easily modified for optimizing hypersonic scramjet inlets.[12] Keeling[13] has also developed an optimization strategy for designing wind-tunnel nozzle contours, which also uses the PNS equations. This approach selects a design based on the optimal convex combination of prospective contours or basis functions. The advantage of this method is that the Jacobian of the objective function, with respect to the design parameters, does not have to be formed. Both CFD-based design techniques yielded example designs that had minimum freestream disturbances according to computational evaluation.

Unfortunately, major upgrades of Langley's hypersonic facilities, including the replacement and refurbishment of most of the nozzles, had been recently undertaken before these design methods were available. This reduced the opportunity to demonstrate the capabilities of the new design methods. Recognizing the importance of improving the flow quality of hypersonic wind-tunnel nozzles, the authors proposed a project where the surplus nozzles of recent facility upgrades at Langley could be used to demonstrate the LS PNS design method at minimum cost. A computer program[14] was developed to implement the design procedure given in Ref. 9. To validate the CFD-based design procedure, two new hypersonic helium wind-tunnel nozzles were designed and tested in Langley's 22-in. helium tunnel.

22-in. Helium Tunnel

The 22-in. helium tunnel is part of the Hypersonic Facilities Complex (HFC) located at NASA Langley Research Center. The helium tunnel is an intermittent, closed-cycle blowdown tunnel that became operational in 1960. The tunnel is supplied with helium from a 5000-psi storage facility that can be heated up to 1100°R using an in-line electric heater. A typical run time for the facility is 15–45 s. The nozzles are approximately 10 ft long, and the test-section diameter is 22 in. Five nozzles were originally fabricated for this facility: three axisymmetric contoured nozzles designed to produce Mach 18, 22, and 26 flows, and two conical nozzles to produce Mach 20 and 40 flows. A new axisymmetric contoured Mach 20 nozzle was designed in 1989 and installed in 1992. This nozzle was designed using a classical MOC–BL correction method. The same basic mechanical design as for the previous nozzles was used, except that the nozzle coordinates were machined using much tighter tolerance.[15] Flowfield surveys for the original Mach 22 nozzles are given by Arrington et al.[16] and more recently by Miller.[17] Flowfield surveys for the contoured Mach 20 nozzle are presented by Miller.[15] The pitot-pressure profile variation at the test section for the Mach 22 nozzle was approximately 9 and 10% at total pressures of 1000 and 2000 psi, respectively, for a 0.5-in. probe spacing. The pitot-pressure profile variation at the test section for the newer Mach 20 nozzle was approximately ±2.8% and ±5.6% at a total pressure of 1500 and 3200 psi, respectively, for a 0.125-in. probe spacing.

All of the contoured nozzles are composed of four sections (Fig. 2) and have a nominal length of approximately 130 in. The original Mach 18, 22, and 26 nozzles were designed and fabricated to minimize both the fabrication cost and the work required to change the nozzles. All three nozzles used the same final two sections—in other words, only the first two sections were unique for each Mach number; the final two sections were the same for all the original nozzles. With the introduction of the new Mach 20 nozzle, the original Mach 18, 22, and 26 nozzles were no longer needed. The Mach 18 and the Mach 22 nozzle were remachined in 1993 using coordinates obtained from a LS PNS optimization procedure to be described later.

The facility was calibrated by making pitot pressure measurements in the test section. A special rake was constructed to provide calibration data using pitot-probe spacing of 0.125 in. over a 20-in. span (Fig. 3). The higher-resolution survey rake is necessary to accurately determine the location and magnitude of freestream disturbances.

Experimental Data Reduction and Uncertainty

The facility's data acquisition system consists of a computer (workstation) that is interfaced with an analog-to-digital (A/D) converter and an electronically scanned pressure (ESP) system. The A/D converter is used to process the stagnation pressure measurement made with a piezoresistive silicon sensor and the stagnation temperature measurement made with an iron-constantan thermocouple. The ESP system is used to measure the pitot pressure in the

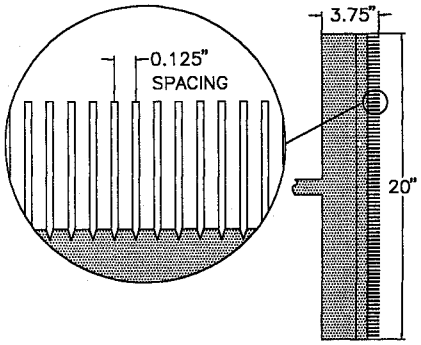

Fig. 3 High-resolution calibration rake.

test section with piezoresistive silicon sensors which are calibrated before each experiment. The value of pitot pressure used for calculating mean flow properties represents the average of the 73 pressure probes spanning ±5 in. from the test-section centerline. Freestream and post-normal-shock thermodynamic and transport properties are determined from real-gas relationship[18] assuming an isentropic expansion through the nozzle.

The error uncertainty associated with the experimental data is derived from the measurements of stagnation pressure, stagnation temperature, and pitot pressure. The uncertainty of the stagnation pressure measurements consists of the following components: instrument accuracy ±2 psi, A/D conversion ±1 psi, and engineering-unit conversion ±1 psi. The root sum square of these components provides an overall uncertainty of ±2.45 psi for the stagnation pressure. The uncertainty of the reservoir temperature measurements comes from the same sources, as follows: instrument accuracy ±2°F, A/D conversion ±0.5°F, and engineering-unit conversion ±1.26°F. The root sum square of these elements provides an overall uncertainty of ±2.42°F for the stagnation temperature. The uncertainty of the pitot pressure measurements is provided by the vendor as an end-to-end system uncertainty, which is stated as ±0.05% full scale (±0.015 psi for this experiment). Note that the data symbols used in the figures of this paper are slightly larger than the data uncertainty. All of these uncertainty levels were verified by in-place calibrations immediately prior to initiating the nozzle flowfield calibration experiments; all measurements were within these worst-case boundaries. The cumulative effect of these measurements results in an uncertainty of ±0.02 in Mach number at $M = 14.6$ and ±0.038 at $M = 20$.

Numerical Methods

CFD calculations for the nozzles are made using the code described in Ref. 14. The nozzle is divided into two regions for computational efficiency: the subsonic–transonic section and the supersonic–hypersonic section. In the subsonic–transonic section, the full Navier–Stokes (NS) equations are solved using a second-order accurate explicit upwind algorithm. In the supersonic–hypersonic section, the parabolized Navier–Stokes (PNS) equations are solved using a second-order accurate explicit upwind algorithm. The following subsections will describe minor modifications made to improve the numerical flow calculations used in the nozzle design.

Real-Gas Modifications for Helium

To accurately simulate the flowfield in many hypersonic tunnels operating at high stagnation pressures and temperatures, the nonideal behavior of the test gas must be included. The nonideal behavior for helium occurs at high densities, in which case the molecules occupy an appreciable fraction of the available volume. The thermal equation of state has to be modified to include this behavior. The simple procedure given by Korte et al.[19] for use with nitrogen is extended for use with helium.

Thermal Equation of State

The thermal equation of state has to include the effect of the volume fraction occupied by the molecules. This effect is extremely important for obtaining the correct nozzle mass flow. The effect is significant in the subsonic to low supersonic sections of the nozzle, where using the ideal-gas equation would resultin an error of up to 9% error in density. The first term of the van der Waals equation of state compensates for the volume fraction of a molecule:

$$p = \frac{\rho RT}{1-\rho b} \tag{1}$$

The advantage of this form of the thermal equation of state is that it is a simple modification of the ideal gas law and is numerically efficient to implement. If b is computed in the p–T domain of interest, the density can be computed in the range of interest of helium tunnel operation with an error of less than 0.3% for the Mach 20 test conditions. Using tabulated values for helium, the value of the gas constant b was computed to be

$$b = 2.83 \times 10^{-3}\ \mathrm{m^3/kg} \tag{2}$$

Excellent agreement is obtained on comparison of the computed compressibility factor with the tabulated values.

Transport Properties for Helium

A modified power-law equation was used to define the viscosity as a function of temperature:

$$\frac{\mu}{\bar{\mu}} = \frac{(T/\bar{T})^{0.648}}{1 + (0.83\,\mathrm{K})/T} \tag{3}$$

where

$$\bar{\mu} = 2.015 \times 10^{-5}\ \mathrm{kg/m \cdot s}, \qquad \bar{T} = 298\,\mathrm{K} \tag{4}$$

The denominator corrects the viscosity at the low freestream temperature achieved at the higher Mach numbers. The conductivity was defined using the computed value of the viscosity and the relationship for the Prandtl number. The Prandtl number was assumed to be at a constant value of 0.67, and the specific heat at constant pressure was fixed at $c_p/R = 2.5$.

Transformation to Computational Coordinates

The physical domain is transformed into computational space using a generalized transformation,

$$\xi = \xi(x, y), \qquad \eta = \eta(x, y) \tag{5}$$

where ξ represents the streamwise direction and η the crossflow direction.

The nozzle wall radius or height, $y_w(x)$, is defined using a set of points, coefficients to a spline, or an analytical expression. For a given streamwise location, Robert's stretching transformation can be used to cluster points either at the wall only or at the wall and the centerline.[20] Unfortunately, for the very thin boundary layers typically found in the throat region, neither one of these stretching functions is satisfactory. If points are only clustered near the wall, an insufficient number of points are at the centerline and the solution deteriorates there. Likewise, if points are stretched at both the wall and the centerline, an insufficient number of points are located in the middle of the domain to accurately compute the flowfield. To overcome this problem, two different stretching functions can be blended together using a fourth-order polynomial in $\bar{\eta}$.

This transformation is given by

$$\frac{y(j)}{y_w(x)} = (1-\bar{\eta}^4)\left\langle 1 - \beta_c + \frac{2\beta_c}{1 + [(\beta_c+1)/(\beta_c-1)]^{1-\bar{\eta}}} \right\rangle + \bar{\eta}^4\left\langle \beta_w - \frac{2\beta_w}{1 + [(\beta_w+1)/(\beta_w-1)]^{\bar{\eta}}} \right\rangle \tag{6}$$

$$\bar{\eta} = \frac{j-1}{j_{\max}-1} \tag{7}$$

The coefficient β is a positive number greater than one. The closer β is to one, the more clustered the grid becomes. The first line of Eq. (6) clusters the points at the centerline according to the value of

β_c, and the second line clusters the points at the wall according to β_w. The clustering at the centerline was fixed at $\beta_c = 1.02$, while the clustering at the wall was allowed to vary in the PNS calculations to maintain the first point off the wall in the linear sublayer of the turbulent boundary layer.

Turbulence Modeling

Turbulent flow is simulated using algebraic turbulence models of either Baldwin and Lomax[21] or Cebeci and Smith.[22] In a recent paper, the analysis[19] of hypersonic wind-tunnel nozzle flowfields has shown the importance of resolving the turbulence BL in the throat region and the necessary grid requirements. In this study, the Baldwin–Lomax model was used in the subsonic–transonic portion of the nozzle and the Cebeci–Smith (CS) model in the supersonic–hypersonic portion. The CS model is difficult to use in the subsonic approach section because of the difficulty in finding the edge of the velocity boundary layer due to variation of the inviscid velocity profiles. However, the edge of the boundary layer is easily determined downstream of the throat. Experience with the models has demonstrated that the displacement thickness in the hypersonic portion of the nozzle is overpredicted more by the Baldwin–Lomax model than by the CS model.

CFD Comparison with MOC–BL Mach 20 Nozzle

Although hypersonic wind-tunnel nozzles are usually geometrically simple, the accurate prediction of measured flowfield parameters has been extremely difficult. Few comparisons of computations with wind-tunnel flowfield measurements have been made for Mach numbers greater than 10. Some of the difficulties have been that 1) nozzle coordinates have not been well defined or accurately machined, 2) the wall temperature distribution is not accurately known, 3) real-gas behavior due to vibrational excitation, high pressure, and high-temperature gas chemistry effects were not included, and 4) the state of BL is unknown (i.e., laminar, transitional, or turbulent). Another problem has been that previous CFD codes were not able to resolve the wall geometry in enough detail to simulate imperfections in the wall design. To improve wind-tunnel nozzle design, actual flow disturbances in existing wind tunnels must be predicted or there will be little hope of improving the nozzle design with CFD-based optimization.

As part of a major facility upgrade, the 22-in. helium tunnel received a new nozzle designed with a classical MOC–BL correction technique. Many of the above-mentioned difficulties in simulating nozzle flowfields are minimized when the nozzle uses helium. Helium can be expanded from room temperature, which means the tunnel wall temperature will be approximately room temperature. The only real-gas behavior of any significance is the effect of high pressure, which is easily included (see above). This nozzle (we will refer to it as MOC-20) was machined using minimum tolerances and a detailed set of coordinates. The first two sections of the nozzle (subsonic section +25.5 in. downstream of the throat) were machined to ±0.0005 in. The third section was 46.5 in. long and was machined to an accuracy of ±0.001 in. The last section was 52 in. long and was machined to an accuracy of ±0.002 in. The sections of the nozzle were assembled in the machine shop, allowing the joints to be hand worked to help minimize joint disturbances. The nozzle was installed in the facility without disassembly.

The MOC-20 nozzle was calibrated over the facility operational range using approximately 60 runs. For each run, the test-section pitot pressure profiles were obtained using the high-resolution pitot survey rake. For a given operating condition, the facility data have shown that within instrument accuracy, the nozzle flow characteristics are repeatable. Overall, the MOC-20 nozzle had better flowfield uniformity than the original nozzles. However, comparisons between the data taken on the original nozzles and the MOC-20 nozzle can be misleading, since pressure measurements were never acquired on the original nozzle using the high-resolution pitot rake, which would have captured disturbance peaks more accurately.

Two cases were computed for comparison: 1) run 4, $p_t = 1505$ psi and $T_t = 547$°R, and 2) run 46, $p_t = 3023$ psi and $T_t = 496$°R. For the first case, input parameters were varied to assess the numerical accuracy of the computed solution. Both cases were computed assuming the flow to be fully turbulent and the wall temperature constant at 530°R.

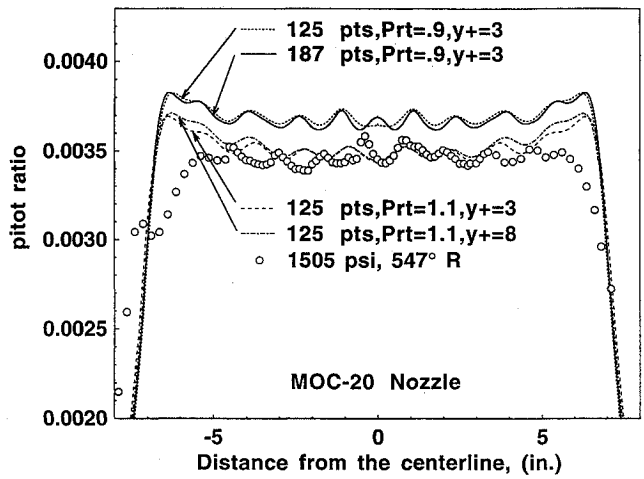

Fig. 4 Comparisons of computed solutions and experimental data.

The subsonic–transonic Navier–Stokes solution was computed on a 81 × 125 grid, where the inflow centerline Mach number was approximately 0.18 and the exit centerline Mach number was 1.8. The grid was clustered at the wall using a fixed value of $\beta_w = 1.0001$. The flowfield was initialized using a one-dimensional solution. The density residual for the solution was reduced six orders of magnitude, converged to a value of less than 10^{-10} in 40,000 iterations, and took approximately 4000 CPU seconds on a Cray Y-MP. Local time stepping was used to advance the solution.

The supersonic–hypersonic PNS solution was started using a Navier–Stokes solution data plane downstream of the throat, where the centerline Mach number was approximately 1.5. The grid was clustered at the wall to maintain the value of y^+ at a point off the wall to less than or equal to 3 by varying the value of β_w between 1.0001 and 1.08. The solution took approximately 2000 CPU seconds to march 1,250,000 planes to reach the rake location. The rake was located approximately 15 in. downstream of the nozzle exit.

The pitot-pressure ratio computed on different numerical grids and using different values of the turbulent Prandtl number are compared with the experimental data in Fig. 4. The computed pitot pressure ratio was calculated by using the ideal-gas relationship for p_{t2}/p_{t1} multiplied by the ratio of the local total pressure to the total pressure on the centerline. The survey rake was positioned in a horizontal orientation. Run 4 is close to the nozzle design stagnation conditions of $p_t = 1500$ psi and $T_t = 530$°R. For this design condition, the nozzle produced a Mach number of only 18.6.

The first calculation used 125 points, and the typically used value of the turbulent Prandtl number was 0.9. The computed pitot-pressure distribution predicts the oscillations in the data; however, the mean value was overpredicted by approximately 6%. Note that a 6% difference in pitot pressure is approximately equal to a 2% difference in Mach number for helium. In the second calculation, the number of points in the crossflow plane was increased from 125 points to 187. The increased resolution gave the same mean value with a slightly more sharply defined pitot disturbance. The third calculation used 125 points and a value of 1.1 for the turbulent Prandtl number. This improved the agreement such that the mean value and the disturbance frequency matched extremely well for the data taken on the right side of the rake. Recall that the turbulent Prandtl number has been measured between 1.5 and 0.5, with 0.9 being the most widely used value in calculations.[23] The agreement near the edge of the boundary layer was not as good, reflecting the simplicity of the turbulence model used and the approximations made in using the PNS equations. The final case shows the effect of varying β_w to maintain a maximum value of y^+ below 8 (instead of 3) in the PNS calculations. Nearly identical results were obtained from the centerline out to approximately 3 in., with minor differences noted out to the edge of the boundary layer. This decreased the CPU time by almost a factor of 5 for the PNS calculations.

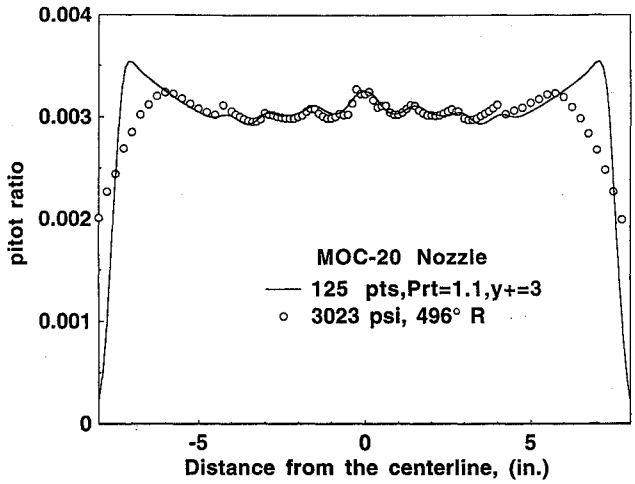

Fig. 5 Comparisons of computed solution and experimental data.

The above results demonstrate that accurate solutions to the governing equations are obtained using 125 points in the radial direction and the effect of maintaining a y^+ of 8 instead of 3 is insignificant in the center core flow region.

Using the same procedure as above, the second high-pressure case was also simulated. A comparison of the computed pitot-pressure distribution with experimental measurements for run 46 is given in Fig. 5. The wind-tunnel nozzle should have the best flow quality at an operating condition near the design Mach number. This high-pressure case yielded a core Mach number of approximately 19.5. Unfortunately, the flow disturbances increase in amplitude with increasing total pressure.

The agreement between the computed pitot-pressure distribution and the measured flowfield survey data demonstrated that the disturbances measured were created by the actual contour design. Hence, the CFD calculations were able to predict disturbances associated with the contour design, and a CFD-based design procedure should be able to improve the flow uniformity.

Nonlinear Least-Squares Optimization

The assumption is made that the shape of the subsonic–transonic contours of the nozzle has been specified and that a NS solution has been computed for this section. The LS PNS optimization procedure used in Ref. 14, including minor modifications used in this study, is presented below.

Objective Function

A nonlinear optimization problem is solved to determine the design parameters by minimization of an objective function. We consider the minimization of an objective function, *Obj*, which is dependent on a set of design parameters, $\boldsymbol{X}$, and is constructed from a series of functions, f_I, of the nonlinear LS form[24]

$$Obj(\boldsymbol{X}) = \sum_{I=1}^{m} f_I^2(\boldsymbol{X}) \tag{8}$$

It is convenient to define vectors

$$\boldsymbol{f} = [f_1, f_2, \ldots, f_m]^T \tag{9}$$

$$\boldsymbol{X} = [X_1, X_2, \ldots, X_n]^T \tag{10}$$

so that the objective function can be written as

$$Obj(\boldsymbol{X}) = \boldsymbol{f}^T(\boldsymbol{X})\boldsymbol{f}(\boldsymbol{X}) \tag{11}$$

For each particular minimization problem, a number of different possibilities exist for the definition of $\boldsymbol{f}$. It is desirable that $\boldsymbol{f}$ be selected so that *Obj* has a sharp minimum and satisfies the design criteria. Recall that the MOC design procedure requires the centerline Mach number M_{axis} and the condition of parallel flow at the design Mach number M_{design} at the nozzle exit. The same requirements are used here to form an objective function. The components of $\boldsymbol{f}$ at the nozzle exit associated with the error in axial Mach number, M_x, and flow angle, ϕ, are

$$f_I = \mathsf{W}_M[(M_x)_{i_{\max},j} - M_{\text{design}}] \tag{12}$$

$$f_{I+1} = \mathsf{W}_\phi(\phi_{i_{\max},j} - 0) \tag{13}$$

and along the centerline

$$f_{I+2} = \mathsf{W}_{MA}[(M_x)_{i,1} - M_{\text{axis}}] \tag{14}$$

where W_M, W_{MA}, and W_ϕ are weighting functions used to adjust the relative tolerances between the different types of error terms. The $i_{\max}$, j index identifies one of the grid points used to evaluate $\boldsymbol{f}$ at the exit of the nozzle and the i, 1 index of a point on the nozzle centerline.

Design Parameters for Wall Contour

Like the objective function, the selection of the design parameters depends on the problem being solved. The ideal set would contain the minimum number of elements and be strongly coupled to the objective function. The design parameters are usually coefficients used to define a wall boundary or quantities that define the flowfield conditions. For the design of a nozzle, the flow conditions are usually given, and the wall contour needs to be determined.

For a contoured nozzle, there is no obvious choice of a function to describe the geometry that would minimize the number of design parameters. A contoured nozzle can have an arbitrary expansion up to the inflection point. After the inflection point, the nozzle contour is determined so that the proper wave cancellation occurs and parallel flow is obtained at the exit of the nozzle. Many contoured nozzles have a curvature discontinuity at the inflection point, i.e., the second derivative is not continuous. In Ref. 6, a cubic spline with five knots was used to model the contoured nozzle. The total number of knots on the spline and the design parameters necessary for defining the contoured nozzle are dependent on how accurately the design problem is to be determined. The nozzle contour is specified using N polynomial equations:

$$\begin{aligned} x_0 < x \le x_1: \quad & y_w = a_0 + a_1 x + a_2 x^2 + a_3 x^3 + a_4 x^4 \\ & + p_5 x^5 + p_6 x^6 \\ x_1 < x \le x_2: \quad & y_w = a_5 + a_6 x + a_7 x^2 + a_8 x^3 \\ & \vdots \\ x_{N-1} < x \le x_N: \quad & y_w = a_{4N-3} + a_{4N-2} x + a_{4N-1} x^2 + a_{4N} x^3 \end{aligned} \tag{15}$$

The first equation is a sixth-order polynomial, where the first three coefficients prescribe the initial radius, slope, and curvature. The last two coefficients in the first equation, p_5 and p_6, are determined as part of the optimization problem. Originally, in Refs. 9 and 14, the first equation was also treated as a cubic. The new formulation has the advantage that the surface curvature can be specified at the beginning, allowing the complete nozzle design to have continuous curvature. In addition, it was found that a sixth-order polynomial equation very closely approximated the inviscid wall shape in the throat region for a nozzle designed using the method of characteristics and the same centerline Mach-number distribution. The N equations result in $4N + 3$ coefficients, assuming that the locations x_1 through x_N are known. The requirement of continuity of the surface, slope, and curvature at x_1 through x_N specifies $3(N-1)$ of the coefficients. The remaining $N+6$ coefficients are specified by using the inlet radius, the slope, the curvature, p_5 and p_6 (from solution to the optimization problem), and the exit radius and slope, and by specifying the slope at $N-1$ locations. Once the above constants are fixed, a linear system of equations is solved to determine the value of the coefficients $a_0 - a_{4N}$.

Wind-Tunnel Nozzle Design and Optimization

To validate the CFD-based design procedure, two new contours were designed to fit inside existing (surplus) nozzles for the 22-in. helium tunnel. An unconstrained optimization problem was solved to determine the nozzle contour design. A Mach 20 contour was

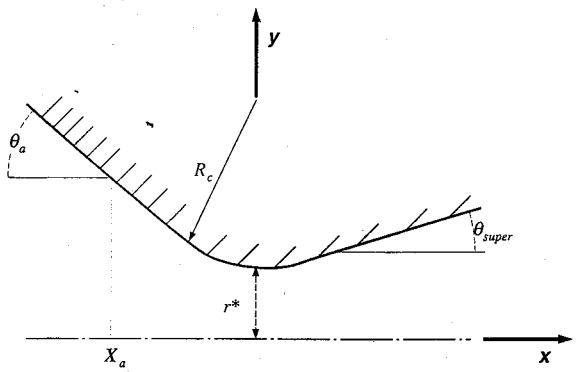

Fig. 6 Geometry of continuous-curvature throat section.

designed to fit within the original Mach 22 nozzle by selecting a specific centerline Mach-number distribution. The Mach 20 design condition was selected so that a comparison could be made with the new MOC-20 nozzle. Likewise, a Mach 14.6 nozzle contour was designed to fit within the original Mach 18 nozzle sections with a new downstream leg (sections 3 and 4 in Fig. 2). A Mach 14.6 design condition was selected, based on a maximum mass flow rate, which sized the throat area. We will refer to these two new nozzles as CFD-20 and CFD-15 for their method of design and approximate design Mach number. The new nozzles were designed for a stagnation condition of 1500-psi pressure and 530°R temperature. The flow was assumed to be fully turbulent, and the nozzle wall temperature was assumed to be a constant 530°R. The nozzle flowfield was computed using a procedure as described for the MOC-20 nozzle. However, the PNS calculations were started at a lower centerline Mach number of 1.18. This is the minimum Mach-number value with which the PNS calculations should be started for helium gas when using Vigneron's pressure splitting (see Ref. 14) with a safety factor of 0.85. In addition, a constant turbulent-Prandtl-number value of 0.9 was used because the nozzle designs were completed before the data were available from the MOC-20 nozzle calibration data discussed earlier.

Subsonic–Transonic Nozzle Design

The subsonic–transonic nozzle design was specified so that the contour would fit within the existing material available for machining. The Mach 18, 22, and 26 nozzles were originally designed with a 45-deg inlet cone connecting to a throat with a small-radius-of-curvature section on the subsonic side; a short, near-constant-area section; and then a rapidly expanding section. This original design limited the number of possible contour designs that would maintain continuous curvature through the throat region for the approximate nozzle throat radius. Sivells[11] recommends that wind-tunnel nozzles be designed with a continuous curvature to minimize difficulties in machining and flowfield disturbances.

The geometry of a continuous-curvature throat section used in the current design is given in Fig. 6. To connect the subsonic side of the throat section to the 45-deg entrance cone, the subsonic contour was specified using the equation[25]

$$\frac{y_w}{r^*} = C_1\left[1 - \exp\left(-\frac{(x/r^*)^2}{2C_1R_c}\right)\right] + 1 \tag{16}$$

where

$$C_1 = R_c \tan\theta_a \exp(1) \tag{17}$$

and the point of intersection with the entrance cone is

$$X_a/r^* = -R_c \tan\theta_a \sqrt{\exp(1)}. \tag{18}$$

A small portion of the downstream contour also has to be specified so that a Navier–Stokes solution can be obtained for the subsonic–transonic section. This can be specified using a polynomial equation, Eq. (16) with a different θ coefficient, or a throat design obtained using Sivells' MOC design code. The selection of the method is not critical in the overall design, since only a small fraction of it is used in the design. The important selection was the combination of r^*, R_c, and θ_{super} that would fit within the existing steel castings. The actual value of r^* could be approximated for the Mach 20 design condition (based on experience with the MOC-20 nozzle) and was specified for the Mach 14.6 nozzle based on maximum mass flow rate. In fact, the Mach 14.6 design point was actually specified after preliminary CFD flow calculations had been run to determine the test Mach number for the design stagnation condition. Table 1 gives the appropriate throat geometry that would fit within the surplus nozzles and still maintain continuous curvature. Tables 2 and 3 give the locations, radii, and slopes of the spline knots used to design the nozzles. Note that the first spline starts at approximately a distance of $r^*/3$ downstream of the throat.

Table 1 Nozzle throat geometry

Nozzle	θ_a, deg	r^*, in.	R_c/r^*	θ_{super}, deg
CFD-20	45	0.325426	3	12
CFD-15	45	0.615737	3	11

Table 2 CFD-15 nozzle: spline node locations

x, in.	y, in	y'
0.263701	0.630974	9.788061E−2
1.525251	0.843863	0.192924
9.087398	2.332012	0.186049
12.97064	3.009324	0.164173
15.58904	3.423812	0.152520
18.07252	3.789795	0.142447
20.71983	4.154172	0.133021
26.25531	4.843187	0.116636
32.58477	5.534029	0.102312
39.96028	6.239124	8.937345E−2
51.50455	7.176921	7.394001E−2
70.10364	8.379585	5.650081E−2
89.34409	9.340702	4.414601E−2
121.5	10.417	2.058827E−2

Table 3 CFD-20 nozzle: spline node locations

x, in.	y, in	y'
0.137684	0.334031	0.112285
0.627653	0.421181	0.201747
4.591949	1.274295	0.208833
5.431093	1.445362	0.199450
6.069334	1.570762	0.193455
7.646309	1.864583	0.179641
9.456063	2.177363	0.166343
13.87087	2.853377	0.141716
20.39345	3.696979	0.118753
30.39771	4.768570	9.730487E−2
41.28461	5.743170	8.263238E−2
53.32363	6.666145	7.135695E−2
76.33926	8.125300	5.636986E−2
124.	10.417	4.414015E−2

Supersonic–Hypersonic Nozzle Design

The supersonic–hypersonic portion of the nozzles was designed by solving an optimization problem. The optimization problem was to find the design parameters (for defining the wall) that minimized the variation of the objective function (defined along the centerline and at the nozzle exit). The nozzle wall was modeled using a spline defined by 14 nodes (Tables 2 and 3). The first interval of the spline used a sixth-order polynomial curve, and the other intervals used cubic polynomials. There were 15 design parameters, which included the slopes at each node after the first, and p_5 and p_6 from Eq. (15). The location of the second node was selected to be slightly upstream of the source flow region (see Ref. 14 for discussion of the nozzle source flow region). The third point was located slightly downstream of the source flow region. A number of points were clustered at the end of the source flow region to model the local change in curvature at the start of the turning contour. The first node's radius, slope, and curvature were held constant to maintain consistency with the subsonic–transonic contour. The exit radius was held constant while the exit slope was optimized. The calculations assumed that the nozzle was connected to an existing

Table 4 Nozzle centerline Mach-number distribution

Nozzle	M_E	M_B	M_C	Length, in.
CFD-20	1.811	15.0	20.0	124.0
CFD-15	1.5325	10.875	14.6	121.5

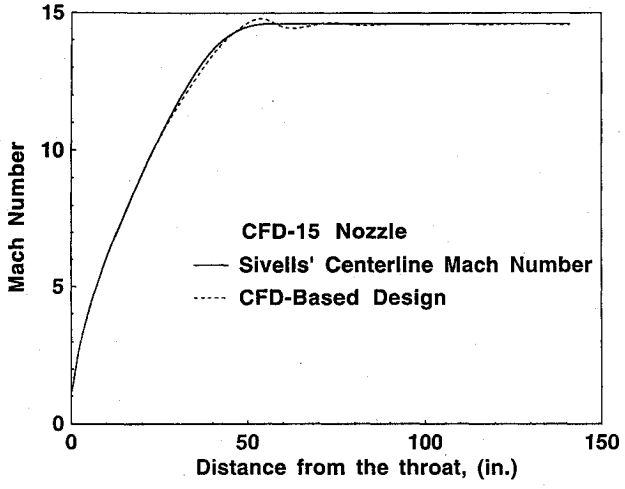

Fig. 7 Comparison of centerline Mach number.

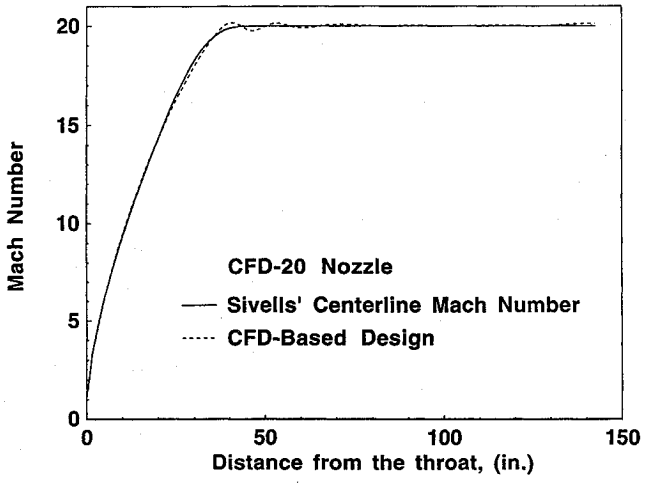

Fig. 8 Comparison of centerline Mach number.

closed test section whose contour was compensated for BL growth. The calculations were stopped 16 in. downstream of the nozzle exit, the approximate location of the survey rake.

The objective function along the centerline consisted of the difference between the computed Mach number and the Mach number based on Sivells' centerline distribution at 100 evenly spaced points. The inputs for defining the centerline Mach-number distribution used to design the two nozzles are given in Tables 1 and 4. The objective function also included the difference between the computed Mach number and the design Mach number as well as the flow angle in the inviscid core for the last solution station computed (which was in the test section). The weighting functions w_M, w_ϕ, and w_{MA} were set at $4/M_{\text{design}}$, 10, and $1/M_{\text{axis}}$, respectively, for the nozzle designs.

The first iteration in the optimization problem required 16 different flowfield solutions to generate the sensitivity derivatives used in determining the Jacobian matrix (see Ref. 9). The Broyden update procedure for the Jacobian matrix was then used for the next four iterations, which only required one flowfield solution each. First, a preliminary design was determined using only 63 points in the crossflow plane. The final design was made using 125 points in the crossflow plane. Once an optimum solution had been determined for the nozzle contour, the subsonic–transonic portion was recomputed with the new nozzle design. The new initial data planes were then used to perform a final design. The optimized nodal slopes and their radii for the two designs are given in Tables 2 and 3. Each nozzle

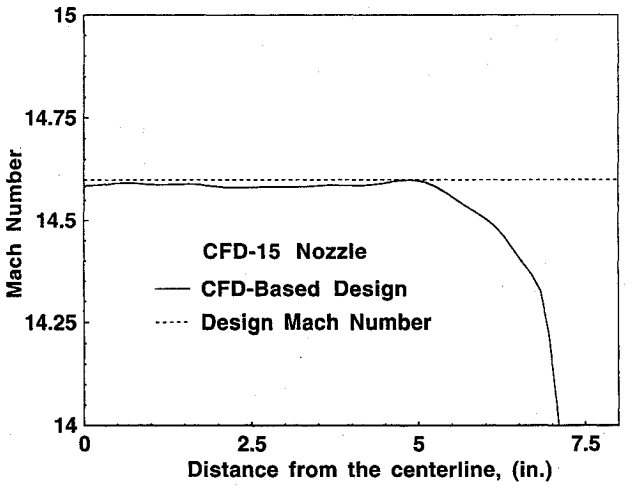

Fig. 9 Comparison of test-section Mach number.

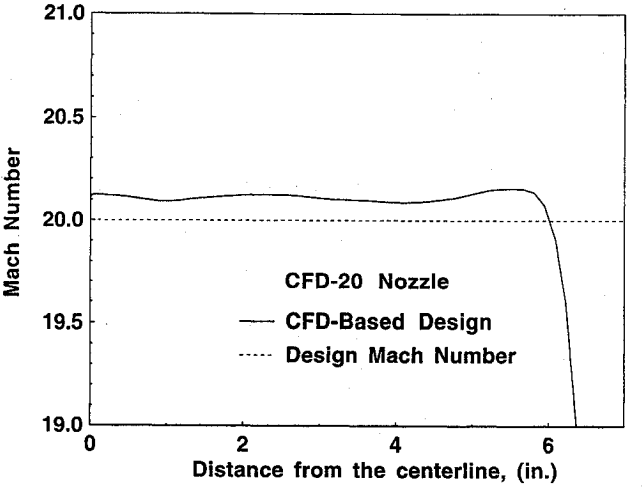

Fig. 10 Comparison of test-section Mach number.

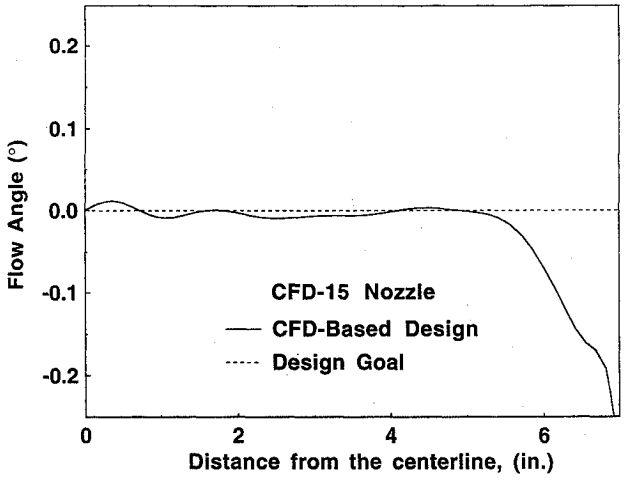

Fig. 11 Computed test-section flow angle.

design (including all iterations) took approximately 20 h of CPU time on a Cray Y-MP supercomputer.

The comparison of the computed centerline Mach number distribution with Sivells' distribution is given in Figs. 7 and 8. The computed test-section Mach-number distribution is given in Figs. 9 and 10, and the flow angle in Figs. 11 and 12. Excellent agreement has been obtained between the computed and the desired nozzle flow conditions. The computed Mach-number contours for the two nozzles demonstrate a smooth expansion and an extremely uniform core region (Figs. 13 and 14). A significant improvement is seen on comparing the computed Mach-number contours of the CFD-20 nozzle and the MOC-20 nozzle.

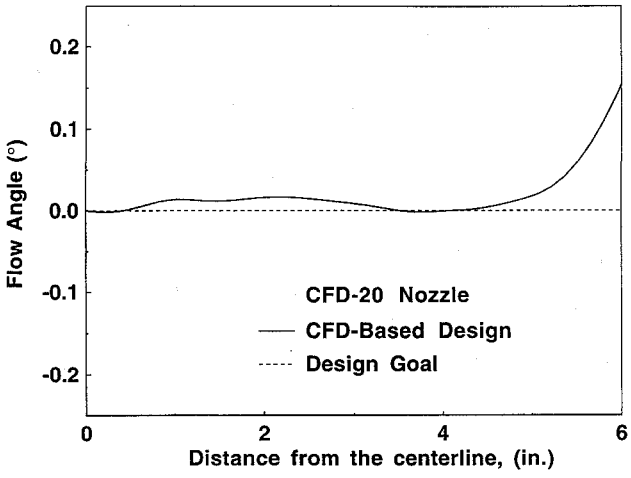

Fig. 12 Computed test-section flow angle.

Experimental Measurement of Flow Quality

To determine if the flow quality of hypersonic wind-tunnel nozzles could be improved in practice using the CFD-based design method, a nozzle had to be designed, manufactured, and tested. To do this, the optimized nozzle designs determined above were machined into the surplus nozzles using the same tolerances mentioned previously for the MOC-20 nozzle. Installing the reworked nozzles into the 22-in. helium tunnel required that they be disassembled at the second and third joints, which had not been required for the MOC-20 nozzle. A preliminary set of test-section pitot surveys has been made over the facility operational range using the high-resolution survey rake to determine the nozzle flowfield uniformity.

CFD-15 Nozzle

The first nozzle to be tested was the CFD-15 nozzle. All cases to be discussed were run at nominal stagnation conditions of 1200-psi pressure and 520°R temperature. The measured pitot-pressure profiles for two runs with different rake orientation (horizontal and vertical) are compared with the computational values in Fig. 15. The rake was located 14.875 in. downstream of the nozzle exit. There

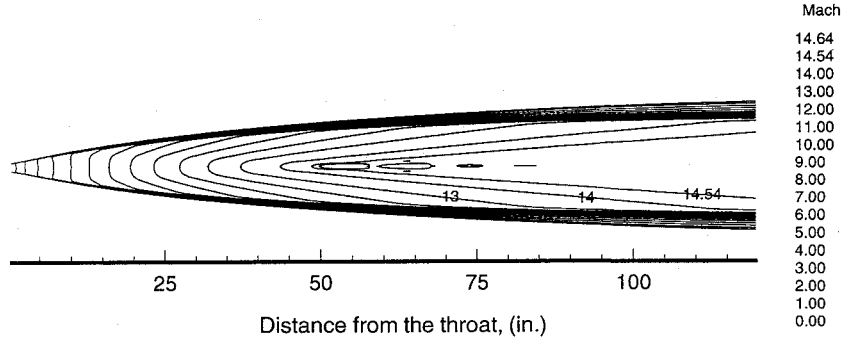

Fig. 13 Computed Mach-number contours for the CFD-15 nozzle (nonlinear contour scale).

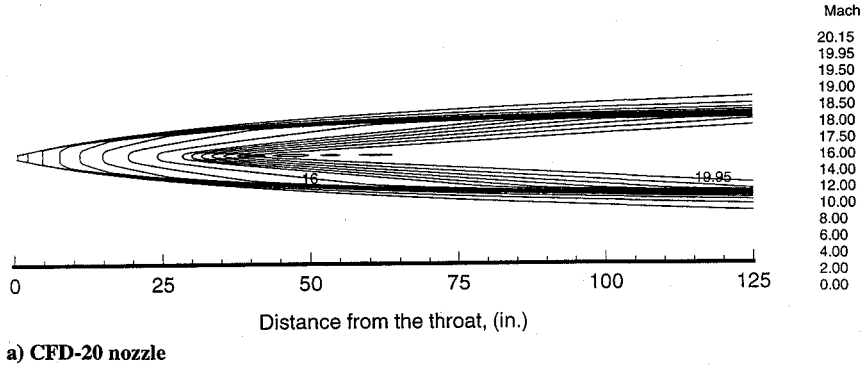

a) CFD-20 nozzle

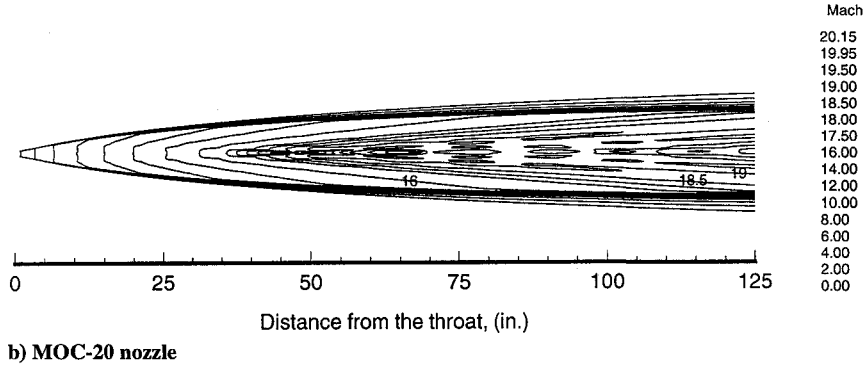

b) MOC-20 nozzle

Fig. 14 Comparison of computed Mach-number contours (nonlinear contour scale).

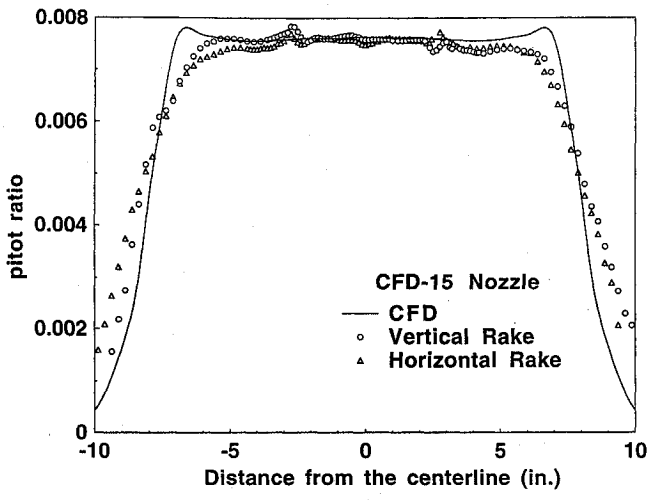

Fig. 15 Comparison of pitot-pressure profile at the test section.

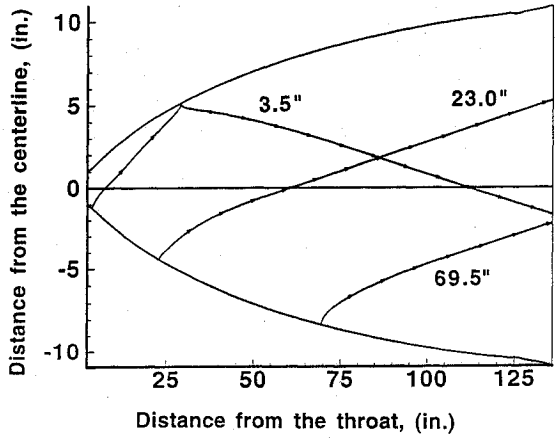

Fig. 16 Computed Mach lines for the CFD-15 nozzle for each joint location.

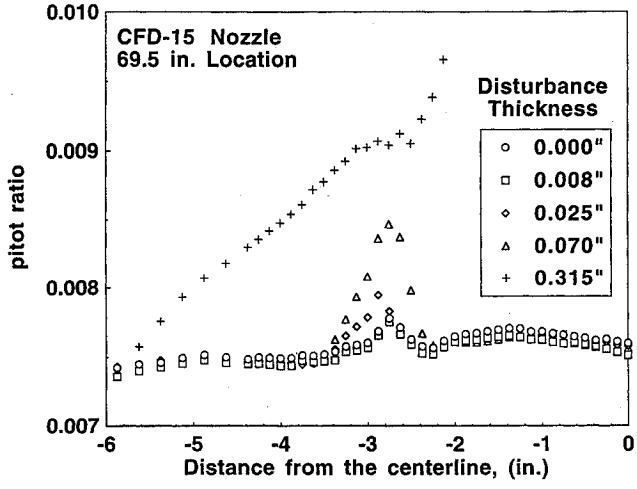

Fig. 17 Comparison of measured pitot profiles for different-size artificial disturbances.

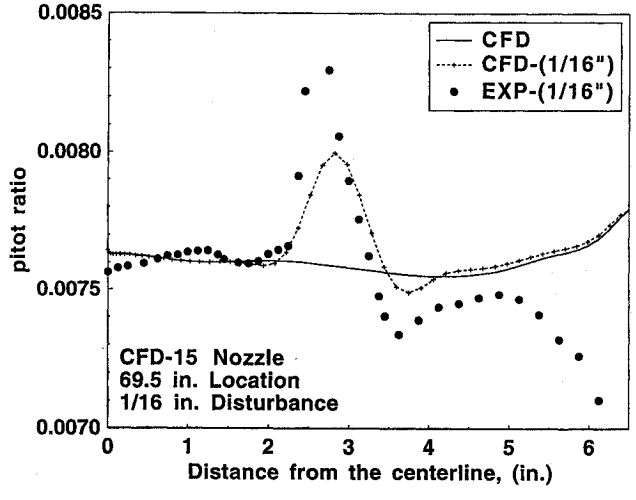

Fig. 18 Comparison of pitot-pressure profiles.

was excellent agreement between the computed and the measured mean value of the pitot pressure in the core flow region. This was also true at the design stagnation conditions, where the nozzle produced the design Mach number of 14.66. The agreement near the edge of the boundary layer was not as good, reflecting the simplicity of the turbulence model used and the approximations made in using the PNS equations. In general, the overall distribution is much smoother than the MOC-20 nozzle. However, the measured pitot-pressure distribution has two anomalies. First, the measured pitot-pressure profile for the vertical rake orientation is asymmetric, appearing to run downhill, whereas the horizontal rake orientation appears to be symmetric. Second, a disturbance is observed centered at approximately ±2.5 in. from the centerline. The asymmetric anomaly is clearly a three-dimensional effect, possibly due to temperature stratification or buoyancy effects during the initial expansion in the throat region, and is beyond the scope of this investigation. The symmetric anomaly was of most concern, since this could be the result of a poor contour design. To determine the origin of the symmetric disturbance, a joint computational and experimental investigation was undertaken.

This sharp localized disturbance led the authors to suspect the problem to be one of the three joints between the four nozzle sections, located 3.5, 23.0, and 69.5 in. downstream of the throat. The joints at 23.0 and 69.5 in. could be reached by crawling into the nozzle from the test section. The Mach lines from each joint were traced using the computed flowfield to the rake location in Fig. 16. The Mach line coming from the joints at 3.5 and 69.5 in. intersected the measurement plane near the area of the disturbance.

To investigate the sensitivity of the nozzle to joint disturbances, a combinational experimental and computational study was made. A layer of electrical tape, 0.75 in. wide and approximately 0.008 in. thick, was first applied to the joint at 69.5 in., and multiple layers of tape and different-size tubing were subsequently tested. The leading edge of the tape (or tubing) was aligned with the downstream edge of the joint. The measured results for the artificial disturbances are shown in Fig. 17 for the rake located 14.875 in. downstream of the nozzle exit. The disturbance from the joint at 69.5 in. was located almost exactly on top of the measured disturbance. Note that there was no significant difference between the untaped nozzle pitot profile and the case with one layer of tape. A noticeable difference was obtained with three layers of tape and with the 1/16-in.-diam tubing. This result was confirmed by simulating a disturbance caused by the 1/16-in. tube at the 69.5-in. joint (Fig. 18). The comparison of computed and measured pitot-pressure disturbance showed that the location was accurately predicted but that the amplitude was low. This is not surprising, since the disturbance was simulated as a gradual ramp up and then down from the original contour. One could conclude from the measurements that the disturbance should be of the order of 0.025 in. A contour variation of this size should have been noticeable to the touch. However, the area around the 69.5-in. joint appeared smooth to the touch, and it had also been tested for possible leakage.

To assess if the disturbance was indeed emanating from the 69.5-in. joint, the rake was moved upstream to determine the direction of propagation. If the disturbance moved outward along the Mach line given in Fig. 16, it would have to be coming from the joint located at 69.5 in. The comparison of pitot distributions for the two rake locations is shown in Fig. 19. A significant drop in pitot pressure is observed on the centerline for the rake in the upstream location. The disturbance peaks also moved towards the centerline when the rake was moved upstream, therefore eliminating the 69.5-in. joint as the origin of the disturbances.

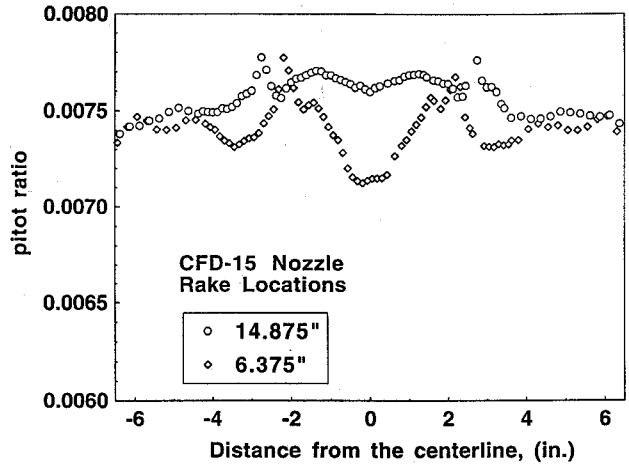

Fig. 19 Comparison of measured pitot-pressure profiles.

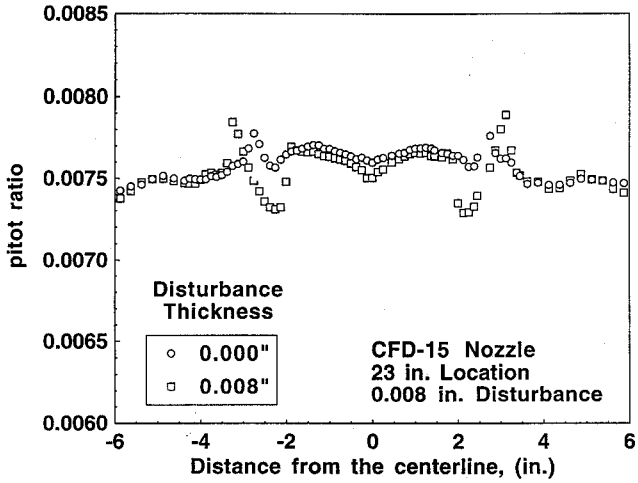

Fig. 20 Comparison of measured pitot-pressure profiles.

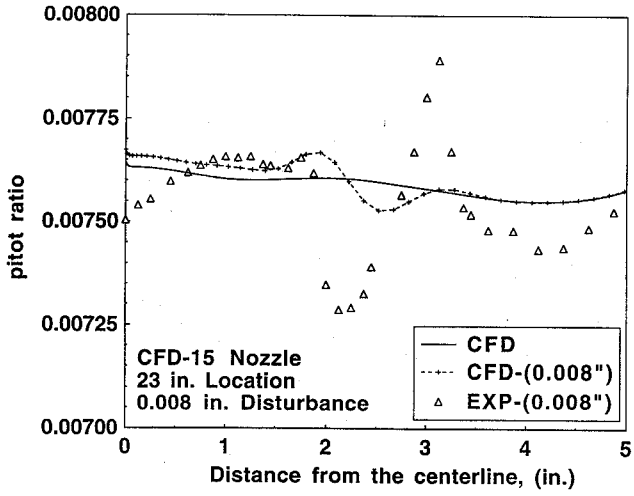

Fig. 21 Comparison of pitot-pressure profiles.

The drop in the pitot pressure at the centerline and the movement of the peaks towards the centerline signals that the disturbance has passed through the centerline at least once. The Mach lines (Fig. 16) for the joints at 3.5 and 23 in. have the proper orientation for causing the measured disturbances. To eliminate the possibility that the joint at 23 in. was causing the disturbance, an experimental and numerical test was conducted. One layer of electrical tape was placed across the 23-in. joint. Figures 20 and 21 show that both the computed and the measured disturbance location caused by the tape were centered about the original disturbance location. Calculations were also made assuming disturbances of different sizes at the 3.5-in.

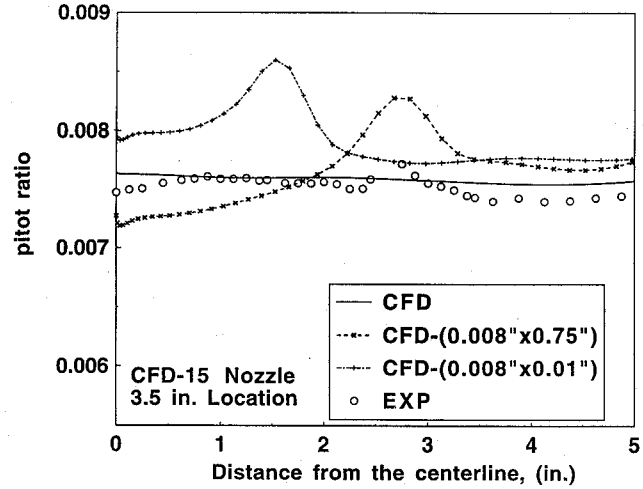

Fig. 22 Computed pitot-pressure profiles.

joint. Figure 22 demonstrates that a wall disturbance of the right size at the 3.5-in. joint also produces a pitot-pressure fluctuation at the same spot as measured with an additional drop in centerline pitot pressure. Therefore, the 3.5-in. and 23-in. joints could both be causing the measured disturbances. The 3.5-in. joint is a press fit, and the 23-in. joint is a flange-type connection. The nozzle was taken apart at the 23-in. joint and examined. There was no obvious problem with the flange or O-ring, and the nozzle was reassembled and tested. The pitot-pressure profiles obtained after reassembly agreed with the previous measurements. The nozzle was removed, and measurements were made to determine differences between the design and the actual contour dimensions, especially near the 3.5-in. and the 23-in. joint locations. The dimensions at both of the two joints were within the machining requirements. However, the 3.5-in. joint did not join perfectly, leaving a 0.0006-in. gap in the contour. The 3.5-in. joint is being refitted to eliminate the gap.

The pitot-pressure measurements and flowfield calculations of the CFD-15 nozzle have shown that the small disturbances observed are most likely due to joint machining and/or a fitting problem. The utility of the CFD in the design has been demonstrated here not only as a method of designing the contour, but as a method to be used in determining the origin of particular disturbances. The variation of measured pitot pressure was on the order of $\pm 2.3\%$, including the disturbances measured, and less than $\pm 1\%$ in the regions outside the disturbances, which agrees with the variation in the CFD prediction. We expect that the measured disturbances can be eliminated or minimized by careful refinishing of the joints.

Usually every attempt is made to locate joints where their Mach lines will not intersect the test region. The joint location of this nozzle was most likely based on the Mach lines for the original Mach 22 nozzle design. It is most unusual to have every joint Mach line converge to the same region in the test section.

CFD-20 Nozzle

The second nozzle to be tested was the CFD-20 nozzle. All the runs to be presented for the CFD-20 nozzle were made at nominal stagnation conditions of 1500-psi pressure and 530°R temperature and with the rake located 14.875 in. downstream of the nozzle exit. The initial runs of the nozzle demonstrated a significant disturbance near the centerline. The second and third joints of the nozzle were inspected, and a thin film of vacuum grease was discovered and cleaned off the second joint. Figure 23 shows the comparison for the pitot-pressure distribution before and after the cleaning. The flow uniformity is significantly improved after the cleaning. Figure 24 compares the experimentally measured pitot profile with the CFD prediction. The CFD prediction was run using a turbulent Prandtl number of 1.1, whereas the original design had been made using the standard value of 0.9. The nozzle produced an average core Mach number of 20.3 at the design stagnation conditions, which was a significant improvement over the MOC-20 nozzle, which reached a Mach number of 18.6 at its design condition. The CFD-20 nozzle measured Mach number could have been closer to the design value

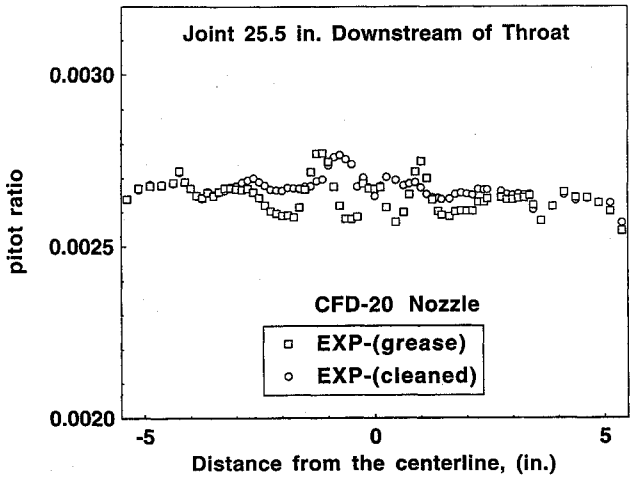

Fig. 23 Comparison of pitot-pressure profiles.

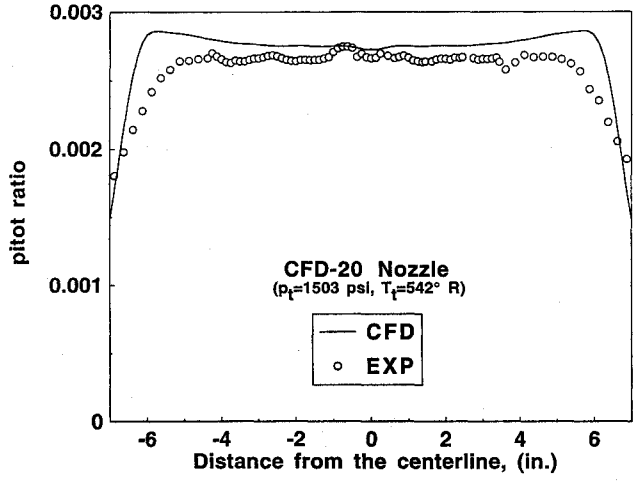

Fig. 24 Comparison of pitot-pressure profiles.

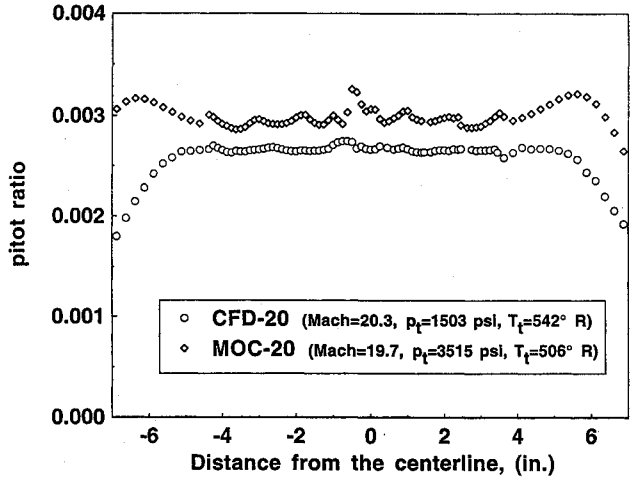

Fig. 25 Comparison of pitot-pressure distributions for nozzles operating near their design Mach number.

if the higher value of the turbulent Prandtl number had been used in the design. Note that while there are still a few isolated fluctuations, the uniformity appears to be fairly smooth. Figure 25 compares the MOC-20 nozzle and CFD-20 nozzle operating near their design Mach number. A significant improvement in flow quality is observed. The CFD-20 nozzle has a core variation of approximately ±3.2% for pitot-pressure measurements, compared to the MOC-20 nozzle variation of approximately ±6.9%. However, the measured pitot-pressure distribution showed variations that are not evident in the computed solution (Fig. 24). The computed pitot-pressure distribution has a core variation of approximately ±1.2%. These are likely also caused by the mechanical joints; a reduction of this variation may be demonstrated in the future by reworking the mechanical joints.

Concluding Remarks

Two hypersonic wind-tunnel nozzle contours have been designed using computational fluid dynamics instead of classical methods. The new contours were machined into surplus nozzle assemblies and tested in NASA Langley's 22-in. helium tunnel. The new computational-fluid-dynamics design technique predicts the design Mach number much more closely than the classical MOC–BL correction technique. Operation of the new nozzles at their design stagnation conditions produced excellent results: The first nozzle matched the design Mach number of 14.6 to within +0.4%, and the second nozzle matched the design Mach number of 20 to within +1.5%; this is a significant improvement over the classically designed nozzle, which missed the design Mach number by −7%. The flow quality in the test section was evaluated using a high-fidelity pitot-pressure rake, which had a probe spacing of 0.125 in. over a 20-in. span. The flow quality of the remachined nozzles showed an improvement over a recently designed and constructed wind-tunnel nozzle based on classical methods. However, the flow quality was not as uniform as the computation design method predicted, because of disturbances emanating from mechanical joints. Both computational and experimental investigations were used to locate the joints believed to be causing the flow disturbances. Excellent agreement was obtained between the measured and computed locations of artificial disturbances placed on the wall. These results demonstrate the practicality of using computational fluid dynamics and computational-based design and optimization procedures for designing and evaluating hypersonic wind-tunnel nozzles and their flowfields. Equally important in future nozzle designs is the location and design of mechanical joints that minimize contour disturbances and accurate machining in the throat and initial expansion region.

References

[1]Anderson, J. D., *Modern Compressible Flow*, 1st ed., McGraw–Hill, New York, 1982, pp. 303–305.

[2]Benton, J. R., "Design and Navier–Stokes Analysis of Hypersonic Wind Tunnel Nozzles," M.S. Thesis, North Carolina State Univ., Raleigh, NC, 1989.

[3]Hackett, C., "Computational and Numerical Analysis of Hypersonic Nozzle Flows with Comparisons to Wind Tunnel Calibration Data," AIAA Paper 92-4011, July 1992.

[4]Benton, J., Perkins, J., and Edwards, A., "Limitations of the Method of Characteristics When Applied to Axisymmetric Hypersonic Nozzle Design," AIAA Paper 90-0192, Jan. 1990.

[5]Candler, G., and Perkins, J., "Effects of Vibrational Nonequilibrium on Axisymmetric Hypersonic Nozzle Design," AIAA Paper 91-0297, Jan. 1991.

[6]Korte, J. J., Kumar, A., Singh, D. J., and Grossman, B., "Least Squares/Parabolized Navier–Stokes Procedure for Optimizing Hypersonic Wind Tunnel Nozzles," *Journal of Propulsion and Power*, Vol. 8, No. 5, 1992, pp. 1057–1063; also AIAA Paper 91-2273, June 1991.

[7]Huddleston, D. H., "Aerodynamic Design Optimization Using Computational Fluid Dynamics," Ph.D. Dissertation, Univ. of Tennessee, Knoxville, TN, 1989.

[8]Korte, J. J., "An Explicit Upwind Algorithm for Solving the Parabolized Navier–Stokes Equations," NASA TP 3050, Feb. 1991.

[9]Korte, J. J., "Aerodynamic Design of Axisymmetric Hypersonic Wind-Tunnel Nozzles Using Least-Squares/Parabolized Navier–Stokes Procedure," *Journal of Spacecraft and Rockets*, Vol. 29, No. 5, 1992, pp. 685–691; Errata, Vol. 29, No. 6, 1992, pp. 870, 871; also AIAA Paper 92-0332, Jan. 1992.

[10]Korte, J. J., "A CFD-Based Aerodynamic Design Procedure for Hypersonic Wind-Tunnel Nozzles," *AGARD Conference Proceedings 514*, 1993, pp. 36.1–36.10.

[11]Sivells, J. C., "Aerodynamic Design of Axisymmetric Hypersonic Wind Tunnel Nozzles," *Journal of Spacecraft and Rockets*, Vol. 7, No. 11, 1970, pp. 1292–1299.

[12]Korte, J. J., and Auslender, A. H., "Optimization of Contoured Hypersonic Scramjet Inlets with a Least-Squares Parabolized Navier–Stokes Procedure," *Computing Systems in Engineering*, Vol. 4, No. 1, 1993, pp. 13–26.

[13]Keeling, S. L., "A Strategy for the Optimal Design of Nozzle Contours," AIAA Paper 93-2720, July 1993.

[14]Korte, J. J., Kumar. A., Singh, D. J., and White, J. A., "CAN – DO—CFD-Based Aerodynamic Nozzle Design & Optimization Program for Supersonic/Hypersonic Wind Tunnels," AIAA Paper 92-4009, July 1992.

[15]Miller, C. G., III, "Hypersonic Aerodynamic/Aerothermodynamic Testing Capabilities at Langley Research Center," AIAA Paper 92-3937, July 1992.

[16]Arrington, J. P., Joiner, R. C., Jr., and Henderson, A., Jr., "Longitudinal Characteristics of Several Configurations at Hypersonic Mach Numbers in Conical and Contoured Nozzles," NASA TN D-2489, 1964.

[17]Miller, C. G., III, "Langley Hypersonic Aerodynamic/Aerothermodynamic Testing Capabilities—Present and Future," AIAA Paper 90-1376, July 1990.

[18]Hollis, B. R., "Real Gas Flow Parameters for NASA Langley 22-Inch Mach 20 Helium Tunnel," NASA CR-4462, Aug. 1992.

[19]Korte, J. J., Hedlund, E., and Anandakrishnan, S., "A Comparison of Experimental DATA with CFD for the NSWC Hypervelocity Wind Tunnel 9 Mach 14 Nozzle," AIAA Paper 92-4010, July 1992.

[20]Anderson, D. A., Tannehill, J. C., and Pletcher, R. H., *Computational Fluid Mechanics and Heat Transfer*, McGraw–Hill, New York, 1984, pp. 247–251.

[21]Baldwin, B. S., and Lomax, H., "Thin Layer Approximation and Algebraic Model for Separated Turbulent Flows," AIAA Paper 78-0257, Jan. 1978.

[22]Cebeci, T., and Smith, A. M. O., *Analysis of Turbulent Boundary Layers*, Academic, 1974, pp. 255–257.

[23]Anderson, D. A., Tannehill, J. C., and Pletcher, R. H., *Computational Fluid Mechanics and Heat Transfer*, McGraw–Hill, New York, 1984, p. 226.

[24]Scales, L. E., *Introduction to Non-linear Optimization*, Macmillan, London, 1985, pp. 110–136.

[25]Beckwith, I. E., private communication, 1990.

J. C. Adams
Associate Editor